

Mo and NiMo catalysts supported on SBA-15 modified by grafted ZrO₂ species: Synthesis, characterization and evaluation in 4,6-dimethyldibenzothiophene hydrodesulfurization

Oliver Y. Gutiérrez^a, Diego Valencia^a, Gustavo A. Fuentes^b, Tatiana Klimova^{a,*}

^a Facultad de Química, Universidad Nacional Autónoma de México (UNAM), Cd. Universitaria, Coyoacán, México D.F., 04510, Mexico

^b Área de Ingeniería Química, Universidad Autónoma Metropolitana-Iztapalapa (UAM-I), Av. Michoacán y Purísima, Iztapalapa, México D.F., 09340, Mexico

Received 2 February 2007; revised 18 April 2007; accepted 21 April 2007

Available online 1 June 2007

Abstract

A series of ZrO₂-containing mesoporous SBA-15 supports and their respective Mo and NiMo catalysts were prepared to study the effect of zirconia loading on the characteristics of Ni and Mo species and their catalytic activity in 4,6-dimethyldibenzothiophene hydrodesulfurization (HDS). ZrO₂-containing SBA-15 solids with different metal loadings (up to 23 wt% of ZrO₂) were prepared by chemical grafting at room temperature. Supports and catalysts were characterized by N₂ physisorption, XRD, UV-vis DRS, TPR, chemical analysis, and HRTEM. The incorporation of zirconia into the SBA-15 support provides better dispersion to the deposited molybdenum species, increasing the effective surface of the MoS₂ phase. Mo and NiMo catalysts supported on SBA-15 materials showed an increase in catalytic activity in 4,6-dimethyldibenzothiophene HDS with zirconia loading in the support. Unpromoted Mo catalysts were active in the formation of hydrogenated intermediates of 4,6-DMDBT, namely tetrahydro- and hexahydrodimethyldibenzothiophenes; however, they were not able to realize efficient sulfur elimination from these intermediates with the formation of desulfurized products. Addition of the Ni promoter resulted in a further increase in Mo dispersion, as well as in the acceleration of C–S bond cleavage in hydrogenated intermediates of 4,6-DMDBT, improving the overall kinetics of the HYD pathway of HDS.

© 2007 Elsevier Inc. All rights reserved.

Keywords: SBA-15; Mesoporous molecular sieves; Zirconia; Chemical grafting; Mo and NiMo catalysts; Deep hydrodesulfurization; 4,6-Dimethyldibenzothiophene

1. Introduction

The demand for high-quality, low-sulfur transportation fuels (gasoline, diesel) is growing with increasing concerns related to public health [1]. Traditionally, the removal of sulfur from petroleum-derived feedstocks has been realized by a hydrodesulfurization (HDS) process using alumina-supported CoMoS and NiMoS catalysts. However, to satisfy new, more stringent environmental restrictions on the sulfur content of fuels, more active HDS catalysts are being requested from industry [2].

Many different approaches have been taken to achieve this goal, including varying the catalyst support. Different materials have been assayed as new supports for HDS catalysts [3,4]. TiO₂ and ZrO₂ have attracted attention due to the greater (by three to five times) intrinsic HDS activity demonstrated by Mo catalysts supported on these oxides compared with their alumina-supported counterparts [3–7]. TiO₂ supports have been widely studied, being the subject of numerous investigations of the support effect in hydrotreating catalysts [3–5]. ZrO₂-supported catalytic systems have been much less widely studied up to now. This neglect is indeed surprising because, as reported previously, Ni-promoted MoS₂ and WS₂ catalysts supported on ZrO₂ show higher hydrodesulfurization and hydrogenation (HYD) activities than titania-supported ones [3,8,9].

* Corresponding author. Fax: +52 55 56225371.

E-mail address: klimova@servidor.unam.mx (T. Klimova).

In general, the high activity observed for the zirconia-supported catalysts is related to the morphology of the sulfided phase. MoS₂ crystallites on zirconia have been found to be shorter and to have less stacking of the layers compared with those on alumina [7,10]. Smaller MoS₂ particles should have a greater number of active sites through increased exposure of MoS₂ crystallite edges. This supposition was confirmed by comparing the amount of Mo active sites in Mo catalysts supported on alumina and zirconia determined by dynamic NO adsorption; five times more NO-adsorbing sites were found in the zirconia-supported catalyst compared with the Al₂O₃-supported counterpart [11]. In addition, it was suggested that zirconia promotes the sulfidation of oxomolybdate entities and promotes the creation of the promoted “NiMoS” phase, which seems to be more accessible to the reactant molecules than in alumina-based catalysts [7,12]. But despite promising results obtained with pure ZrO₂ support, its possible application in catalysts is restricted due to the low surface area (<100 m²/g) and porosity of commercially available zirconia and structural instability during high-temperature treatment. Because of zirconia’s low surface area and despite its high intrinsic activity (per Mo atom), the specific activity (per g of catalyst) of ZrO₂-supported catalysts is lower than that of alumina-supported catalysts [7].

Recently, different zirconia-containing materials suitable for hydrotreating catalysts have been synthesized and tested in HDS reactions. Promising results have been obtained with ZrO₂-containing mixed oxide supports (Al₂O₃-ZrO₂ [11,13,14], ZrO₂-TiO₂ [15], and ZrO₂-SiO₂ [13,16]). Attempts also have been made to prepare pure zirconia supports with ordered mesopore structure or to introduce Zr⁴⁺ species in siliceous mesoporous molecular sieves of different types (e.g., MCM-41, HMS, SBA-15). Zr-HMS materials with different Zr/Si ratios have been prepared and used as supports for Mo HDS catalysts, and showed higher catalytic activity than the reference Mo/SiO₂ material in thiophene HDS [17]. It was found that zirconium improved the hydrogenation activity of the samples and facilitated reduction of the supported molybdenum species. However, MCM-41 and HMS-type materials have poor mechanical and hydrothermal stability [18,19] and relatively small pores (about 20–35 Å diameter), which can be easily blocked by HDS active phases [17,20,21]. Mesoporous silicas of the SBA family seem to be more suited for modification with ZrO₂ because of their larger pores, thicker pore walls, and higher hydrothermal stability compared with MCM-41 [20–23]. Recently, our group prepared a series of TiO₂- and ZrO₂-containing SBA-15 materials and the respective NiMo catalysts and tested them in 4,6-dimethyldibenzothiophene (4,6-DMDBT) HDS [24]. We found that incorporating titania or zirconia in the support provided better dispersion to deposited Ni and Mo active species and increased their catalytic activity in HDS of 4,6-DMDBT, one of the most refractory sulfur compounds. The catalytic activity obtained with ZrO₂-containing supports was greater than that obtained with TiO₂-containing supports, and substantially higher (almost double) than obtained with the reference NiMo/ γ -Al₂O₃ catalyst. Taking this

finding into account, we continue our research of novel HDS catalysts supported on ZrO₂-modified SBA-15 materials.

In the present work, we report some new results on the Zr-SBA-15 support preparation and characterization. To further investigate the cause of the high catalytic activity of the NiMo/Zr-SBA-15 formulations, we attempted to analyze separately the contributions of the ZrO₂-containing support and of the Ni promoter in the catalytic behavior of these systems. For this purpose, a series of SBA-15 materials modified with different amounts of zirconia was prepared by chemical grafting and used to support unpromoted Mo catalysts and Ni promoted ones, both of which were evaluated in the 4,6-dimethyldibenzothiophene (4,6-DMDBT) HDS reaction.

2. Experimental

2.1. Support and catalyst preparation

The siliceous SBA-15 material used in this work has been synthesized as described elsewhere [22,23]. ZrO₂-modified SBA-15 supports were prepared by chemical grafting [24]. Zirconium(IV) propoxide (Zr(*n*-PrO)₄, 70 wt% solution in 1-propanol, Aldrich) was used as the zirconia source, and absolute ethanol was used as the solvent (EtOH, Aldrich, 99.999%). In the grafting procedure, calcined SBA-15 was slurried in EtOH containing Zr(*n*-PrO)₄ for 8 h at room temperature. To eliminate excess Zr(*n*-PrO)₄, the filtered material was washed with dry EtOH. The solid was then dried in air at room temperature and calcined in static air at 550 °C for 5 h. Hereinafter, ZrO₂-containing SBA-15 materials are designated Zr(*x*)SBA-15 samples, where *x* represents the wt% of ZrO₂ in the sample.

To assess thermal stability, the Zr(23)SBA-15 material was calcined at different temperatures (700, 800, 900, or 1000 °C) for 1 h. For the hydrothermal stability studies, the freshly synthesized material [SBA-15 or Zr(23)SBA-15] was refluxed in distilled water (at a water-to-sample ratio of 1 L/g) for 24 h and dried at 100 °C for 24 h before further characterization.

Mo- and NiMo/SBA-15 catalysts were prepared by a standard incipient wetness technique. The calcined supports were impregnated successively using aqueous solutions of ammonium heptamolybdate, (NH₄)₆Mo₇O₂₄·4H₂O (Aldrich), and nickel nitrate, Ni(NO₃)₂·6H₂O (Aldrich). Mo was impregnated first. After each impregnation, the catalysts were dried (100 °C, 24 h) and calcined (500 °C, 4 h). In addition, NiMo catalyst supported on γ -alumina was prepared for comparison purposes. The nominal composition of the catalysts was 12 wt% of MoO₃ and 3 wt% of NiO. Hereinafter, the catalysts are designated as Mo or NiMo/corresponding support.

2.2. Zirconium(IV) deposition isotherm

Equilibrium adsorption experiments were performed at 25 ± 0.1 °C. Siliceous SBA-15 parent material, calcined previously and dried at 120 °C for 15 h, was used as an adsorbent. In each experiment, 1.0 g of the SBA-15 was suspended in 200 mL of the Zr(*n*-PrO)₄ ethanol solution of various concentrations of Zr(IV) ranging between 0.8 × 10⁻⁴ and 2.3 × 10⁻¹ mol/L.

This suspension was kept in inert atmosphere (Ar) under continuous stirring for 8 h, allowing sufficient time to reach the equilibrium of Zr(IV) adsorption. Subsequently, the solid was separated from the liquid by filtration, dried, and calcined as described above. The surface concentration of Zr(IV) atoms in the calcined solid (Γ , atoms Zr/nm²) was calculated from the results of chemical analysis. Zr(IV) loadings obtained from the analysis of the ZrO₂-grafted solids were found to be in good agreement with those calculated on the basis of the difference between zirconium(IV) concentration in the solution before and after deposition using the relationship

$$\Gamma = \{V(C_0 - C_{\text{eq}})\} / WS, \quad (1)$$

where C_0 , C_{eq} , V , W , and S are the Zr(IV) concentration before and after adsorption (mol/L), suspension volume (0.2 L), weight (g), and specific surface area (m²/g) of the support, respectively.

2.3. Support and catalyst characterization

The supports and catalysts were characterized by N₂ physisorption, X-ray diffraction (XRD), UV–vis diffuse reflectance spectroscopy (DRS), temperature-programmed reduction (TPR), SEM-EDX, and high-resolution transmission electron microscopy (HRTEM). N₂ adsorption/desorption isotherms were measured with a Micromeritics ASAP 2000 automatic analyzer at liquid N₂ temperature. Before the experiments, the samples were degassed ($p < 10^{-1}$ Pa) at 270 °C for 6 h. Specific surface areas were calculated by the BET method (S_{BET}), the total pore volume (V_{p}) was determined by nitrogen adsorption at a relative pressure of 0.98, and pore size distributions were determined from the desorption isotherms by the BJH method. The mesopore diameter (D_{p}) corresponds to the maximum of the pore size distribution. The micropore area (S_{μ}) was estimated using the correlation of t -Harkins and Jura (t -plot method). XRD patterns were recorded in the $3^\circ \leq 2\theta \leq 90^\circ$ range on a Siemens D5000 diffractometer, using CuK α radiation ($\lambda = 1.5406$ Å) and a goniometer speed of $1^\circ (2\theta) \text{ min}^{-1}$. Small-angle XRD ($2\theta = 1^\circ\text{--}10^\circ$) was performed on a Bruker D8 Advance diffractometer using small divergence and scattering slits of 0.05° . The a_0 unit-cell parameter was estimated from the position of the (100) diffraction line ($a_0 = d_{100} \times 2/\sqrt{3}$) [25]. Pore wall thickness, δ , was assessed by subtracting D_{p} from the a_0 unit-cell parameter corresponding to the distance between the centers of adjacent mesopores. UV–vis–NIR electronic spectra of the samples were recorded in the wavelength range 200–2500 nm using a Cary 15E spectrophotometer equipped with a diffuse reflectance attachment. BaSO₄ was used as reference. TPR experiments were carried out in an automated ISRI-RIG-100 characterization system equipped with a thermal conductivity detector. In the TPR experiments, the samples were pretreated in situ at 500 °C for 2 h under air flow and cooled in an Ar stream. The reduction step was performed with an Ar/H₂ mixture, with a heating rate of 10 °C/min, up to 1000 °C. The chemical analysis of the Zr-containing SBA-15 supports was performed by Desert Analytics. HRTEM studies were performed using a Jeol 2010

microscope (resolving power 1.9 Å). The solids were ultrasonically dispersed in heptane, and the suspension was collected on carbon coated grids. Slab length and layer stacking distributions of MoS₂ crystallites in each sample were established from the measurement of at least 300 crystallites detected on several HRTEM pictures taken from different parts of the same sample dispersed on the microscope grid.

2.4. Catalytic activity

The 4,6-DMDBT HDS activity tests were performed in a batch reactor at 300 °C and 7.3 MPa total pressure for 8 h. Before the catalytic activity evaluation, the catalysts were sulfided *ex situ* in a tubular reactor at 400 °C for 4 h in a stream of 15 vol% of H₂S in H₂ under atmospheric pressure. The sulfided catalysts (0.15 g) were transferred in an inert atmosphere (Ar) to a batch reactor (Parr) containing 40 mL of 4,6-DMDBT solution in *n*-hexadecane (0.024 mol/L). The course of the reaction was followed by withdrawing aliquots each hour and analyzing them on an HP-6890 chromatograph. To corroborate product identification, the product mixture was analyzed on a Hewlett Packard GC-MS instrument.

3. Results and discussion

3.1. Supports

Fig. 1A illustrates the deposition isotherm of Zr(IV) species on the surface of the parent SBA-15 obtained experimentally at room temperature (25 °C). The initial solution concentration of zirconium(IV) propoxide was changed to reach different metal loadings in Zr(IV)-grafted solids. A plateau observed in the isotherm corresponds to the monolayer surface coverage. The experimental points are well fitted with a Langmuir-type isotherm,

$$\Gamma / \Gamma_m = (K C_{\text{eq}}) / (1 + K C_{\text{eq}}). \quad (2)$$

This type of isotherm implies localized Langmuir-type adsorption of the zirconium species on SBA-15 surface with too weak (if any) lateral interactions. Therefore, most of the adsorbed zirconia species should exist in isolated form, and zirconia agglomerates, if exist, should be present in the samples only as a minority fraction. This result points out high dispersion of grafted Zr(IV) species and confirms the conclusion of our previous work in which only isolated Zr(IV) species in tetrahedral coordination were detected on SBA-15 surface by UV–visible diffuse reflectance spectroscopy regardless of ZrO₂ loading [24]. The monolayer capacity (Γ_m) found from linearized Langmuir plot (Fig. 1B),

$$C_{\text{eq}} / \Gamma = 1 / (\Gamma_m \times K) + C_{\text{eq}} / \Gamma_m, \quad (3)$$

was 2.15 Zr(IV) atoms per nm². This value is slightly below the silanol surface density of ~ 3.7 OH/nm² that has been reported previously for SBA-15 material [26]. From the above results, it can be inferred that in the monolayer-like distribution of metal species reached at room temperature, each zirconium atom is retained on the surface by one or two Zr–O–Si

linkages. In addition, the existence of some isolated hydroxyls inert to the interaction with zirconium *n*-propoxide at room temperature also can be expected on the surface of the parent SBA-15 material. To prove this hypothesis, an additional experiment was performed in which Zr(IV) grafting was realized from dry *n*-propanol solution at its boiling temperature (97 °C) for 8 h. In this case, zirconium(IV) loading (24.6 wt% of ZrO₂) was only slightly higher than that obtained at room tempera-

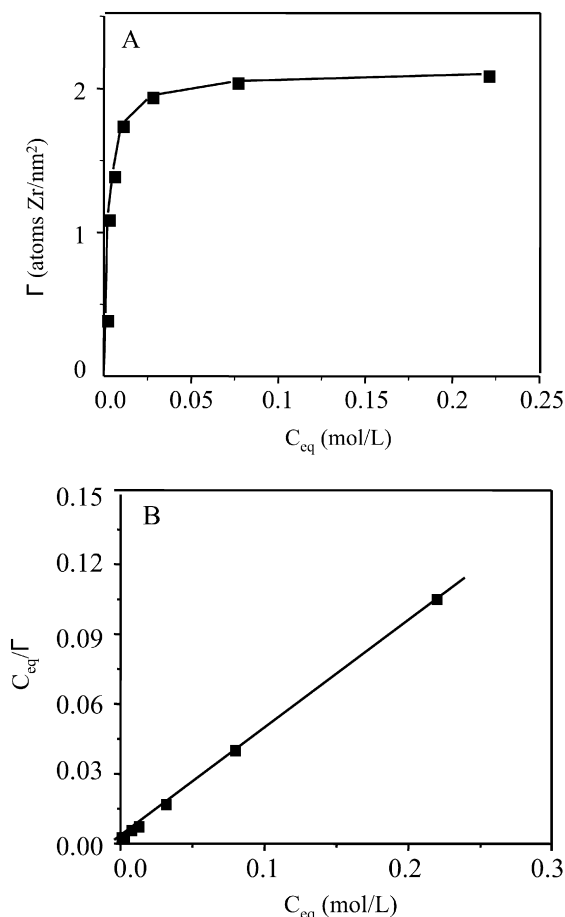


Fig. 1. (A) Variation of the surface concentration of Zr(IV) atoms on SBA-15 with equilibrium concentration of zirconium(IV) *n*-propoxide in dry ethanol at 25 °C. (B) Plot of C_{eq}/Γ against C_{eq} (linearized Langmuir plot).

ture (23.4 wt% of ZrO₂). Therefore, it can be assumed that most surface hydroxyl groups of SBA-15 available for interaction with zirconium(IV) *n*-propoxide react with it at room temperature. Previously it was suggested that SBA-15 materials exhibit a “rough” inner surface containing different types of silanol groups: “isolated” silanol groups, “interacting” SiOH groups (silanols that are close enough to form H-bonds), “geminal” OH groups associated with surface defects (two OH groups attached to the same Q² silicon atom), and “hidden” OH groups located inside of small pores [26]. Because of space requirements of a Zr(IV) *n*-propoxide, accessible OH groups (groups located on the inner surface of SBA-15 mesopores) can be expected to participate principally in the interaction with Zr(IV) species. The probability of the reaction between Zr(*n*-PrO)₄ and “hidden” hydroxyls seems to be much lower. Therefore, it can be assumed that a small amount of unreacted ≡Si–OH groups can still be present inside SBA-15 micropores in the samples covered with Zr(IV) monolayer at room temperature and higher.

The textural and structural characteristics of Zr(*x*)SBA-15 materials are given in Table 1. The parent SBA-15 material shows a surface area of 860 m²/g, a micropore area of 139 m²/g, and a total pore volume of 1.163 cm³/g. Zirconia grafting on the SBA-15 surface results in a decrease of area and pore volume values. Thus, BET surface area decreases to 544 m²/g and micropore area decreases to 102 m²/g after Zr(IV) incorporation. Total pore volume and micropore volume follow similar tendencies after incorporation of Zr(IV) into the SBA-15 support. This decrease can be due to an increase in the density of Zr(*x*)SBA-15 materials with ZrO₂ wt loading. In a previous report [24], we showed that Zr(IV) grafting does not produce changes in the characteristic shape of the SBA-15 isotherm (type IV isotherm with an H1 hysteresis loop), with the exception of some decrease in the amount of adsorbed N₂, indicating that the original pore structure of the parent SBA-15 material is maintained after Zr(IV) incorporation. In addition, small-angle XRD patterns of Zr(*x*)SBA-15 samples were found to be similar to those of parent siliceous SBA-15 [24]. The positions of the reflections characteristic of the *p6mm* hexagonal symmetry of SBA-15 and their intensities did not change after Zr(IV) grafting, indicating that the long-range periodicity order

Table 1
Textural and structural characteristics and chemical composition of Zr(*x*)SBA-15 materials

Sample	ZrO ₂ (wt%) ^a	Zr (atoms/nm ²)	<i>S</i> _{BET} (m ² /g)	<i>S</i> _μ (m ² /g)	<i>V</i> _p (cm ³ /g)	<i>V</i> _μ (cm ³ /g)	<i>D</i> _p (Å)	<i>a</i> ₀ (Å)	δ (Å)
SBA-15	0	0	860	139	1.163	0.054	56	102	46
SBA-15(HT) ^b	0	0	488	65	1.352	0.024	78	104	26
Zr(6)SBA-15	6.2	0.4	751	125	1.026	0.050	56	n.d. ^c	n.d.
Zr(13)SBA-15	13.4	1.1	624	110	0.887	0.048	56	n.d.	n.d.
Zr(17)SBA-15	17.1	1.4	605	108	0.813	0.042	56	102	45
Zr(21)SBA-15	21.1	1.8	583	105	0.769	0.041	56	102	45
Zr(22)SBA-15	22.5	2.0	548	102	0.736	0.040	56	102	45
Zr(23)SBA-15	23.4	2.1	544	102	0.708	0.040	56	102	46
Zr(23)SBA-15(HT) ^b	n.d.	n.d.	540	54	0.788	0.019	57	103	46

^a Determined by chemical analysis.

^b Samples after hydrothermal treatment in boiling water for 24 h.

^c Not determined.

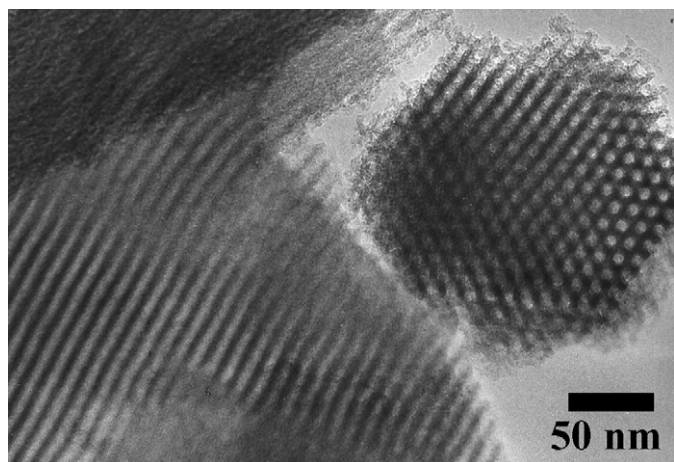


Fig. 2. Transmission electron microscopy image of the Zr(23)SBA-15 support.

of the SBA-15 sample was preserved intact and that its unit cell parameter and pore wall thickness did not change significantly (Table 1).

Fig. 2 shows a TEM micrograph of the Zr(23)SBA-15 support. A well-ordered hexagonal array of mesopores can be seen for this sample when the electron beam is parallel to the main axis of the cylindrical pores. When the electron beam is perpendicular to the main axis, the cylindrical pores are viewed from the side as a striped image. The distance between the centers of two adjacent pores is about 100 Å, and the pore diameter is about 60 Å. The image of the SBA-15 material modified with a monolayer of grafted ZrO₂ species is similar to that reported previously for the parent SBA-15 material [24]. Formation of ZrO₂ agglomerates on the external surface or inside the mesopores of SBA-15 particles was not detected.

To assess the thermal stability of Zr(IV) species grafted on the SBA-15 surface, the Zr(23)SBA-15 support was calcined at different temperatures (between 700 and 1000 °C). The results of powder XRD of the thermally treated samples, displayed in Fig. 3, show that dispersed Zr(IV) species remain immobilized in SBA-15 at calcination temperatures below 800 °C. The formation of tetragonal ZrO₂ crystalline phase (JCPDS card 17-0923) can be clearly seen in samples calcined at 800, 900, and 1000 °C. According to the literature, the tetragonal zirconia phase is metastable and easily transforms into the monoclinic one, which is stable below 1170 °C. Our results demonstrate that the immobilization of zirconia species by grafting on the SBA-15 surface delays the crystallization of ZrO₂ and leads to stabilization of the tetragonal phase of zirconia at room temperature. Previously, it was reported that such an effect can be related to a high dispersion of ZrO₂ particles [11,27].

The hydrothermal behavior of Zr(IV)-grafted SBA-15 materials was also characterized because of its importance for the possible use of these materials in applications associated with aqueous solutions. Previously it was reported that the hydrothermal stability of siliceous SBA-15 is much better than that of MCM-41 which, when subjected to refluxing in water for short periods, readily loses its hexagonal structure and is rendered amorphous [28,29]. Moreover, it was found that even aqueous impregnation of MCM-41 material with cobalt

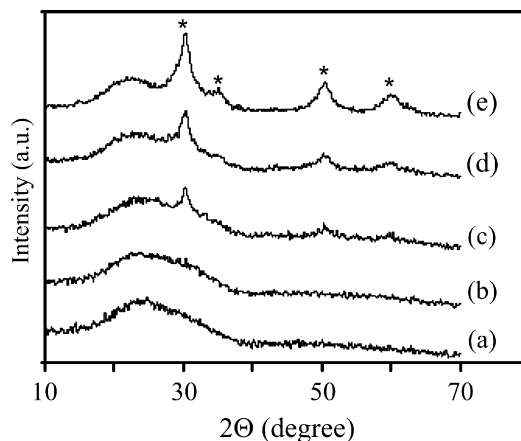


Fig. 3. Powder XRD patterns of Zr(23)SBA-15 sample calcined at different temperatures for 1 h: (a) 550; (b) 700; (c) 800; (d) 900; and (e) 1000 °C. * Tetragonal ZrO₂ (JCPDS card 17-0923).

nitrate solution followed by drying leads to the loss of long-range ordering and a substantial decrease in the surface area and pore volume [20]. The better hydrothermal stability of SBA-15 silica was attributed to its much thicker pore walls in comparison with MCM-41 [22,23]. However, siliceous SBA-15, as well as other amorphous silicas, can suffer some structural destruction of mesoporous framework in boiling water due to the interaction of surface silanol groups with water molecules. Figs. 4 and 5 show nitrogen adsorption–desorption isotherms and small-angle XRD patterns of the SBA-15 and Zr(23)SBA-15 samples before and after hydrothermal treatment in boiling water for 24 h. In general, the N₂ sorption isotherm of siliceous SBA-15 maintains its shape after treatment in boiling water. However, the amount of N₂ adsorbed at relative pressures below 0.6 decreases to almost half that of the untreated SBA-15. In line with this finding, significant decreases in both BET and micropore surface areas are seen (Table 1). These decreases are accompanied by a significant increase in pore diameter from 56 to 78 Å for the sample refluxed for 24 h. Nevertheless, small-angle XRD results (Fig. 5) demonstrate that the thick-wall SBA-15 material retains its structural integrity and long-order pore arrangement after being refluxed. No significant change was found in the unit-cell parameter value of SBA-15 after refluxing. The foregoing results demonstrate that a significant decrease in pore wall thickness (from 46 to 26 Å) occurs during hydrothermal treatment.

Incorporation of zirconia onto the SBA-15 surface by grafting resulted in a significant improvement in hydrothermal stability of the support, as is evident from Figs. 4 and 5. Only a decrease in micropore area and a slight increase in the total pore volume were detected for the Zr(23)SBA-15 sample after refluxing (Table 1). In this case, the BET surface area of the sample was maintained almost the same as before the hydrothermal treatment, indicating that an increase in mesopore area at the expense of micropore area. It seems that only some micropores are sensible for the presence of water molecules. The enhanced stability of SBA-15 due to Zr(IV) grafting can be attributed to the disappearance of most surface ≡Si–OH groups, which can be easily attacked by water molecules, and

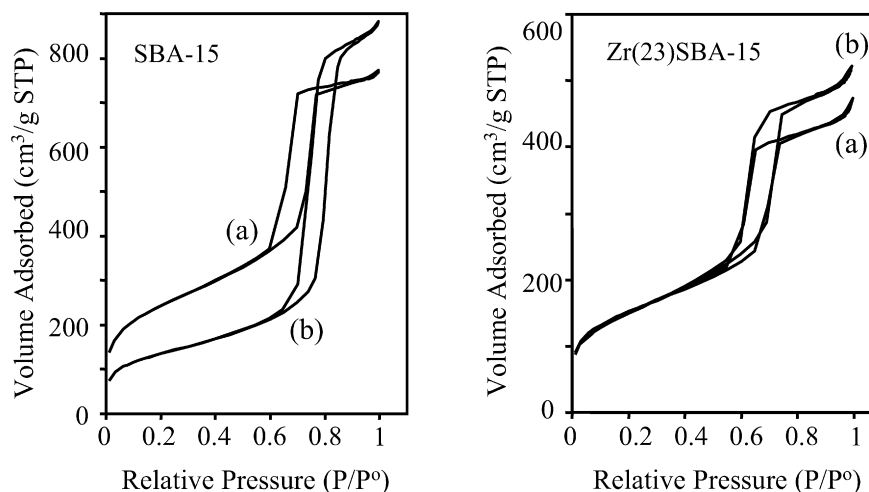


Fig. 4. Nitrogen adsorption–desorption isotherms of siliceous SBA-15 and Zr(23)SBA-15 supports before (a) and after treatment in boiling water for 24 h (b).

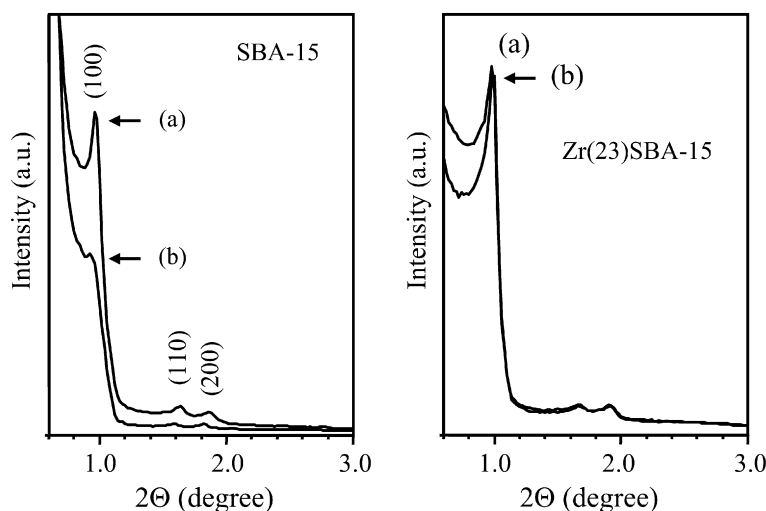


Fig. 5. Small-angle XRD patterns of siliceous SBA-15 and Zr(23)SBA-15 supports before (a) and after treatment in boiling water for 24 h (b).

the appearance of new $\equiv\text{Zr}-\text{OH}$ groups resistant to hydrolysis with water. Similar stabilization of MCM-41 by introducing Al^{3+} species onto its surface has been reported previously and attributed to the creation of “protective surface composite layer” preventing destruction of the silica wall [30].

Returning to the above results, it can be stated that the chemical grafting procedure used in this work allows preparation of Zr-containing SBA-15 materials with high loading (up to 23 wt%) of dispersed ZrO_2 species with no significant damage to the initial SBA-15 structure. The presence of Zr(IV) species grafted on SBA-15 surface significantly improves the hydrothermal stability of the mesoporous molecular sieve, making it attractive for different applications in catalysis.

3.2. Mo and NiMo catalyst characterization

The textural characteristics of Mo and NiMo catalysts supported on SBA-15 molecular sieves are given in Table 2. A significant decrease in BET surface area and total pore volume occurs after incorporation of Mo and Ni into the supports. This decrease is more pronounced for the catalysts supported on

Table 2

Textural and structural characteristics of Mo and NiMo catalysts supported on Zr(x)SBA-15 materials

Sample	S_{BET} (m^2/g)	S_{μ} (m^2/g)	V_{p} (cm^3/g)	V_{μ} (cm^3/g)	D_{p} (Å)	a_0 (Å)	δ (Å)
Mo/SBA-15	601	82	0.851	0.031	55	102	47
Mo/Zr(17)SBA-15	460	60	0.642	0.022	56	102	46
Mo/Zr(21)SBA-15	416	53	0.592	0.019	56	102	46
Mo/Zr(23)SBA-15	394	49	0.596	0.018	54	102	48
NiMo/SBA-15	550	71	0.784	0.026	55	102	47
NiMo/Zr(17)SBA-15	450	53	0.646	0.019	55	102	47
NiMo/Zr(21)SBA-15	378	44	0.552	0.016	54	100	46
NiMo/Zr(23)SBA-15	367	39	0.537	0.014	54	102	46

siliceous SBA-15 (with S_{BET} decreasing to 30% for the Mo catalyst and 36% for the NiMo catalyst) than for the catalysts supported on ZrO_2 -containing materials. No changes were detected in the form of N_2 adsorption–desorption isotherms or in the shape of the hysteresis loop after successive incorporation of Mo and Ni species into the SBA-15 supports (Fig. 6).

In line with this, (100), (110), and (200) reflections of the $p6mm$ hexagonal structure of SBA-15 are still observed in the

small-angle XRD patterns of Mo and NiMo catalysts (Fig. 7). The intensity of these reflections decreases after Ni and Mo incorporation (especially for pure silica SBA-15 support), probably because Mo is a strong X-ray absorber [21] or due to some loss of long-range order of the support mesostructure induced by a partial blocking of its pore channels by Ni and Mo oxidic species. A low dispersion of molybdate species has been detected for mesostructured silica-supported catalysts [2,21,31]. In line with this, powder XRD patterns of Mo and NiMo catalysts supported on siliceous SBA-15 [Fig. 8, curves (a)] reveal the formation of crystalline MoO₃ in orthorhombic phase (JCPDS card 35-609). The intensity of the characteristic XRD signals of MoO₃ decreases with Ni addition. The average size of the MoO₃ crystals, determined using Scherrer's equation, decreases from 961 Å for unpromoted Mo/SBA-15 catalyst to 519 Å for the Ni-promoted one. The size of MoO₃ crystals compared with the pore diameter values of the used SBA-15 material clearly indicates that they should be located on the external surface of the support particles.

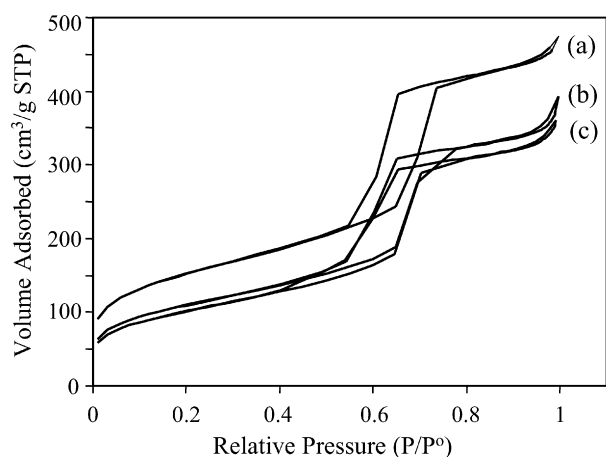


Fig. 6. Nitrogen adsorption-desorption isotherms of: Zr(23)SBA-15 (a); Mo/Zr(23)SBA-15 (b); and NiMo/Zr(23)SBA-15 (c).

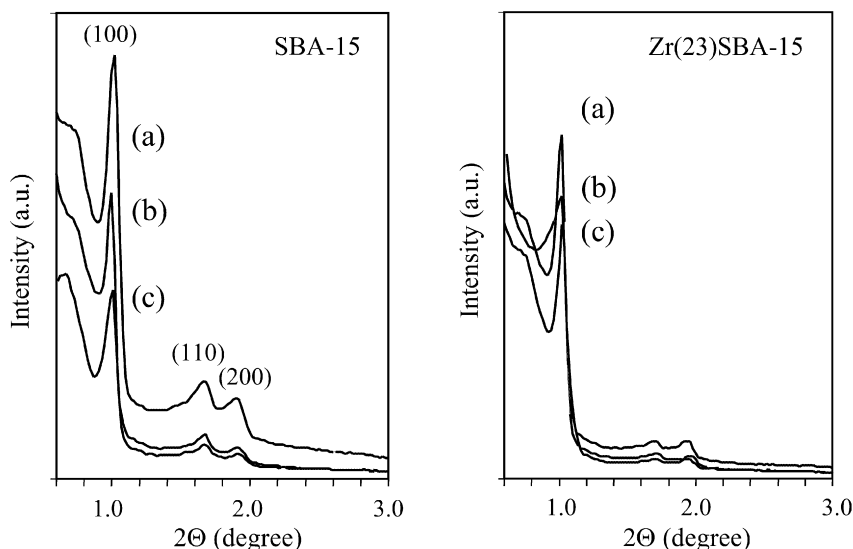


Fig. 7. Small-angle XRD patterns of supports (a); Mo (b); and NiMo (c) catalysts supported on SBA-15 and Zr(23)SBA-15.

Incorporation of Zr(IV) oxide into the surface of SBA-15 seems to improve the dispersion of Mo and Ni species. A decrease in textural characteristics after incorporation of Ni and Mo into Zr-containing SBA-15 supports was not as strong as that for the siliceous SBA-15 (Table 2). Comparing the intensities of the small-angle XRD signals of Zr(23)SBA-15 support with those of corresponding Mo and NiMo catalysts reveals that the effect of Ni and Mo incorporation is much smaller in this case than for the pure silica SBA-15 sample (Fig. 7). The foregoing results allow us to suppose that Ni and Mo oxidic species should be better dispersed on Zr(*x*)SBA-15 materials than on the parent SBA-15. Results from powder XRD characterization of Mo and NiMo catalysts (Fig. 8) confirm this supposition. The diffractograms of unpromoted Mo catalysts clearly show an increase in MoO₃ dispersion with zirconia loading in the support. Low-intensity signals of the orthorhombic MoO₃ crystalline phase can still be observed for the Mo catalyst supported on SBA-15 with 6 wt% of grafted ZrO₂; however, these reflections are not detected for unpromoted Mo catalysts supported on SBA-15 materials with 13 wt% or higher ZrO₂ loadings. Adding nickel to the Mo/Zr(6)SBA-15 catalyst resulted in a further increase in MoO₃ dispersion. The foregoing results from nitrogen physisorption and XRD characterization of Mo and NiMo catalysts clearly show that both zirconium and nickel oxides similarly improve the dispersion of Mo oxidic species on the SBA-15 surface.

UV-vis DRS spectra of Mo, Ni, and NiMo catalysts (Fig. 9) were recorded to obtain more information about Ni and Mo oxidic species. For Mo⁶⁺ species, the absorption due to the O²⁻ → Mo⁶⁺ charge transfer transition occurs in the 200–400 nm range. The exact position of this band depends on the state of molybdenum coordination and aggregation [32–34]; the isolated (tetrahedral) molybdate species show absorption at 250–280 nm, whereas polymolybdate (octahedral) species absorb at 300–330 nm. In addition, both types of Mo species exhibit a second strong absorption band at about 220–230 nm. The DRS spectra of unpromoted Mo catalysts (Fig. 9) show the

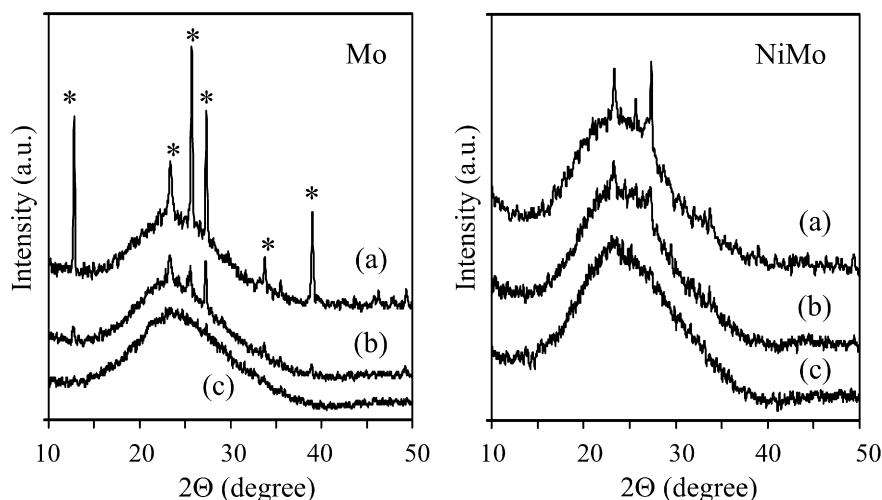


Fig. 8. Powder X-ray diffraction patterns of Mo and NiMo catalysts supported on SBA-15 (a); Zr(6)SBA-15 (b); and Zr(13)SBA-15 (c). * Orthorhombic MoO_3 (JCPDS card 35-609).

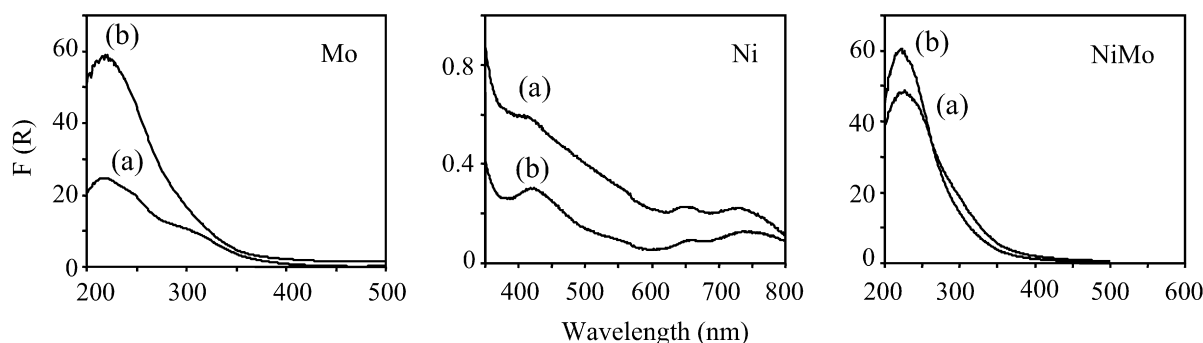


Fig. 9. UV-vis diffuse reflectance spectra of Mo, Ni, and NiMo catalysts supported on SBA-15 (a) and Zr(23)SBA-15 (b). The spectrum of each support was subtracted from the spectrum of corresponding catalyst.

presence of a mixture of Mo^{6+} oxidic species in tetrahedral (T_d) and octahedral (O_h) coordinations. However, the proportions of different types of Mo species change with the composition of the support. Thus, in the spectrum of the catalyst supported on siliceous SBA-15, absorption bands at 300–330 nm ($O_h \text{Mo}^{6+}$) and 250 nm ($T_d \text{Mo}^{6+}$) can be clearly observed. In the spectrum of Mo/Zr(23)SBA-15 catalyst these signals are less defined, whereas absorption in 260–300 nm region increases its intensity.

These changes confirm that the addition of zirconium to the SBA-15 support leads to an increase in the dispersion of O_h molybdenum species and to a decrease in the proportion of the T_d species. The absorption edge energies (E_g) calculated for Mo catalysts are also well in line with the above conclusion. The E_g value of 3.2 eV found for Mo/SBA-15 catalyst is characteristic of the crystalline MoO_3 phase. Meanwhile, a higher E_g value (3.6 eV) of Mo/Zr(23)SBA-15 catalyst indicates an increased dispersion of polymolybdate species. The DRS spectra of Ni/SBA-15 and Ni/Zr(23)SBA-15 catalysts are also shown in Fig. 9. Only the presence of octahedral Ni^{2+} species in the form of NiO (bands at 415, 650, and 730 nm [35]) can be observed for all catalysts, regardless of the support used. Comparing the DRS spectra of unpromoted Mo catalysts and Ni-promoted ones (Fig. 9) demonstrates that adding a Ni promoter leads to

increased dispersion of Mo species in all catalysts. This is indicated by an increase in E_g values after the incorporation of nickel to 3.5 eV for the NiMo/SBA-15 catalyst and 3.7 eV for the catalyst supported on Zr(23)SBA-15. In addition to a blue shift of the band-gap absorption edge, Ni incorporation also produced a significant change in the shape of the DRS spectrum of the Mo catalyst supported on siliceous SBA-15, namely absorption bands at 300 nm (agglomerated polymeric $O_h \text{Mo}$ species) and 250 nm (tetrahedral Mo^{6+} species) become less defined, and absorption at 260–280 nm increases. The changes in E_g value and the spectrum shape induced by Ni addition were not so marked when ZrO_2 -containing support was used. It seems that the effect of Ni addition on the characteristics of the deposited Mo oxidic species is stronger for the pure silica SBA-15 support than for the ZrO_2 -containing one.

The TPR results for Ni, Mo, and NiMo catalysts are shown in Fig. 10. The TPR profile of the Ni/SBA-15 sample exhibits a broad low-temperature reduction region (300–550 °C) that can be clearly ascribed to the reduction of octahedrally coordinated Ni^{2+} species weakly bound to the silica surface [31]. These nickel oxide species are reduced almost completely (98%) to metallic nickel ($\text{Ni}^{2+} \rightarrow \text{Ni}^0$) in a single reduction step. The reduction profile of the Mo/SBA-15 catalyst shows two main reduction peaks at 572 and 740 °C and a shoulder at about

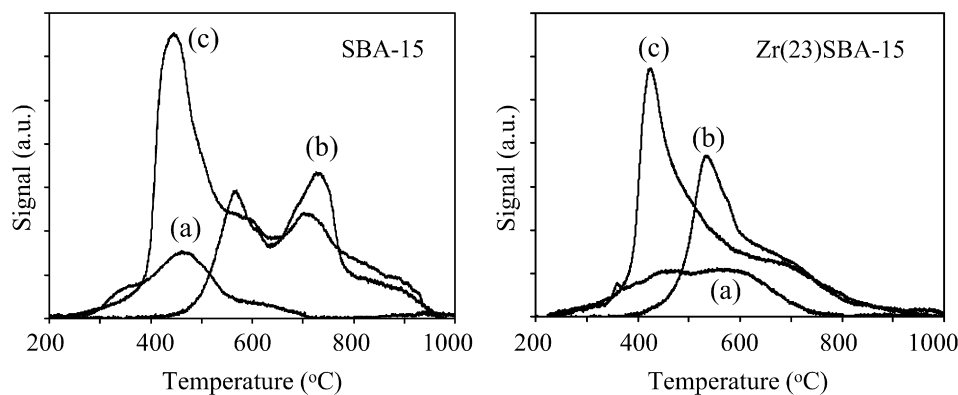


Fig. 10. TPR profiles for Ni (a), Mo, (b) and NiMo (c) catalysts supported on SBA-15 and Zr(23)SBA-15.

614 °C. The low temperature peak (572 °C) is generally associated with the reduction of Mo^{6+} to Mo^{4+} of polymeric octahedral Mo species weakly bound to silica surface (probably small clusters of MoO_3) [36,37]. Comparing the present TPR pattern with that of bulk MoO_3 (main peak at 600–630 °C [37]), hydrogen consumption near 614 °C can be assigned to the reduction of crystalline MoO_3 phase detected by XRD. The peak at about 740 °C in the case of SBA-15-supported Mo catalyst can be ascribed to the second step in the reduction of the polymeric octahedral Mo species (from Mo^{4+} to Mo^0) or to the first step of reduction of isolated tetrahedral Mo^{6+} species in strong interaction with the support [37,38]. It should be mentioned that the intensity of this high-temperature reduction peak in our Mo/SBA-15 catalyst is unusually high compared with the TPR profiles of similar silica-supported catalysts prepared by impregnation of ammonium heptamolybdate solutions (e.g., Mo/SiO₂ [39], Mo/MCM-41 [31]). This can be attributed to the presence of a high proportion of isolated T_d molybdenum species in strong interaction with the SBA-15 surface, probably because of the particular characteristics of this material, such as a high degree of roughness of its inner surface and a great number of surface defects [26]. In the TPR profile of NiMo catalyst supported on SBA-15 the reduction of Mo species occurs at lower temperatures (450 and 714 °C for the first and second steps of reduction of O_h Mo^{6+} species) than in the corresponding unpromoted Mo/SBA-15 catalyst. In addition, hydrogen consumption at 580–600 °C becomes less intense, in line with the increased dispersion of MoO_3 species in the presence of the Ni promoter as detected by XRD.

The TPR profile of Ni catalyst supported on Zr-containing SBA-15 is more complex than that of the Ni/SBA-15 sample (Fig. 10). Two poorly resolved broad reduction peaks can be seen in the TPR of this sample, indicating the presence of at least of two different Ni^{2+} surface species. The low-temperature H_2 consumption region (maximum at 470 °C) can be assigned to the reduction of a NiO-like phase in weak interaction with the support. The intensity of this peak decreases after the incorporation of zirconia onto the SBA-15 surface. At the same time, a new high-temperature reduction peak (maximum at 585 °C) appears in the TPR profile of Ni/Zr(23)SBA-15 sample as a result of the stronger interaction of nickel species with zirconia-containing support. Comparing the TPR patterns

of Mo catalyst supported on SBA-15 and Zr(23)SBA-15 shows that zirconium(IV) grafting onto the SBA-15 surface leads to a slight decrease in the temperature of reduction of octahedral molybdenum species (the first step in their reduction occurs at 540 °C; the second step, at 700 °C). In addition, the incorporation of Zr(IV) into SBA-15 results in disappearance of a peak with a maximum at 740 °C observed in the case of Mo/SBA-15 catalyst and ascribed to the first step in the reduction of tetrahedral Mo^{6+} species. Adding nickel to the Mo/Zr(23)SBA-15 catalyst leads to a further decrease in the temperature of reduction of Mo oxidic species, indicating that the effect of Ni promoter is similar in the siliceous and zirconia-containing SBA-15 supports. It appears that in both cases, this is due to the better dispersion of Mo species in presence of nickel.

HRTEM characterization of sulfided Mo and NiMo catalysts was performed to gain more insight into the dispersion of catalytically active MoS_2 species. Fig. 11 shows HRTEM micrographs of Mo and NiMo catalysts supported on parent SBA-15 and Zr(23)SBA-15. The typical fringes due to MoS_2 crystallites with 6.1 Å interplanar distances were observed on micrographs of all sulfided catalysts. Inhomogeneous dispersion of the MoS_2 phase can be seen in the unpromoted Mo catalyst supported on siliceous SBA-15 (micrograph (a), Fig. 11). MoS_2 crystallites with lengths between 25 and 80 Å and stacking from two to seven layers are formed. In addition, some very large MoS_2 crystals (600–2000 Å) were also found on the external surface of SBA-15 particles. Nickel addition to this catalyst resulted in better dispersion and more homogeneous distribution of MoS_2 crystals (Fig. 11b). Particles with lengths between 40 and 60 Å and stacking from 2 to 5 layers are predominant in this case. Zirconium incorporation in the support leads, as expected, to better dispersion of MoS_2 active phase (Figs. 11c and 11d). Figs. 12 and 13 show the slab length and stacking degree distributions for Mo and NiMo catalysts supported on SBA-15 and Zr(23)SBA-15. It can be clearly observed that ZrO_2 addition in the support leads to a decrease in the stacking degree and length of MoS_2 particles of unpromoted Mo catalysts. Short MoS_2 particles (20–40 Å) with small number of layers (2 or 3) are formed predominantly in the sulfided Mo/Zr(23)SBA-15 catalyst. When Ni is added to the Mo/SBA-15 catalyst, morphology of the sulfided catalyst (stacking degree and slab length) is also changed significantly. However, when Zr(23)SBA-15 is used

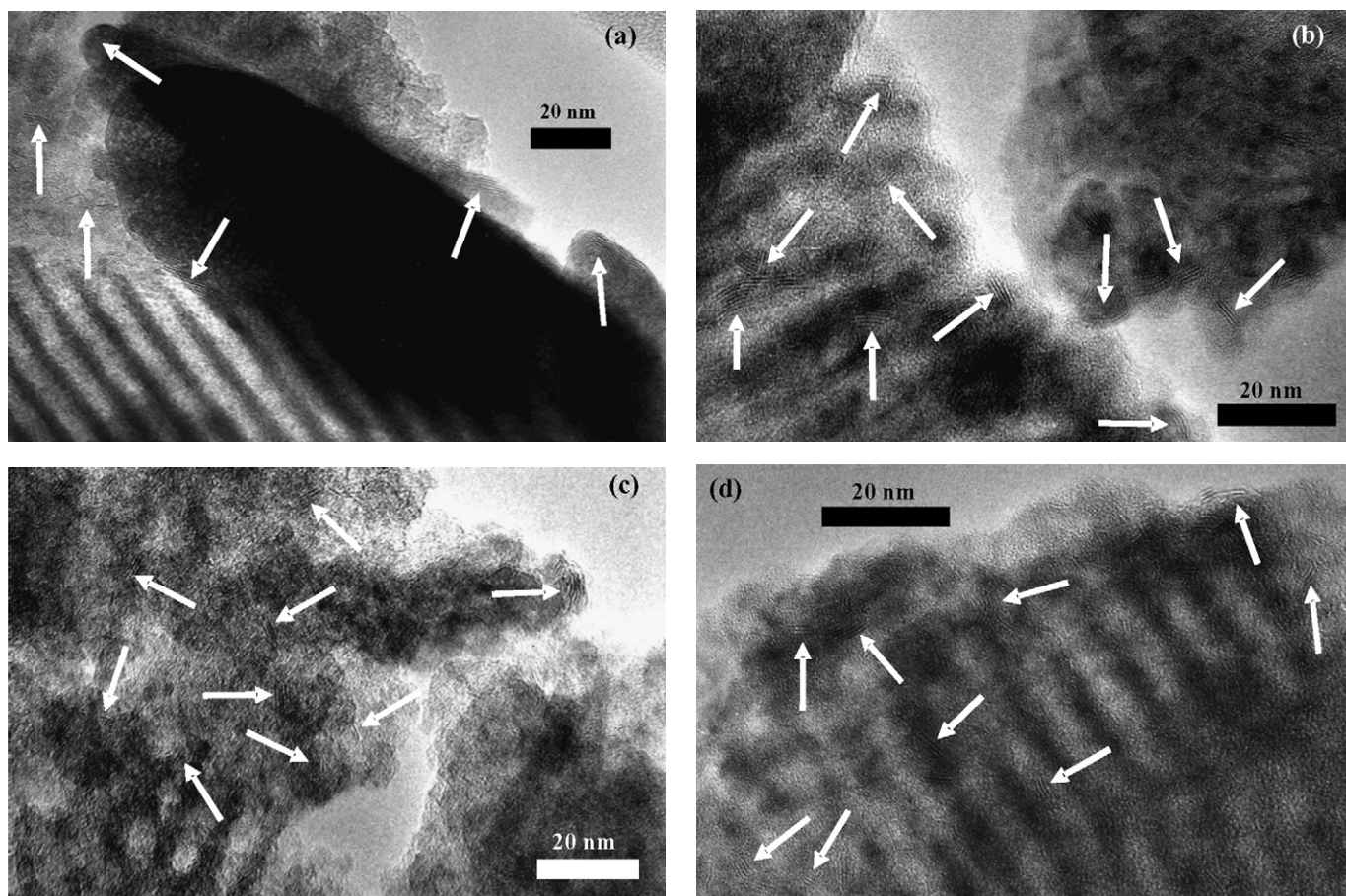


Fig. 11. HRTEM micrographs of sulfided catalysts: Mo/SBA-15 (a); NiMo/SBA-15 (b); Mo/Zr(23)SBA-15 (c); and NiMo/Zr(23)SBA-15 (d).

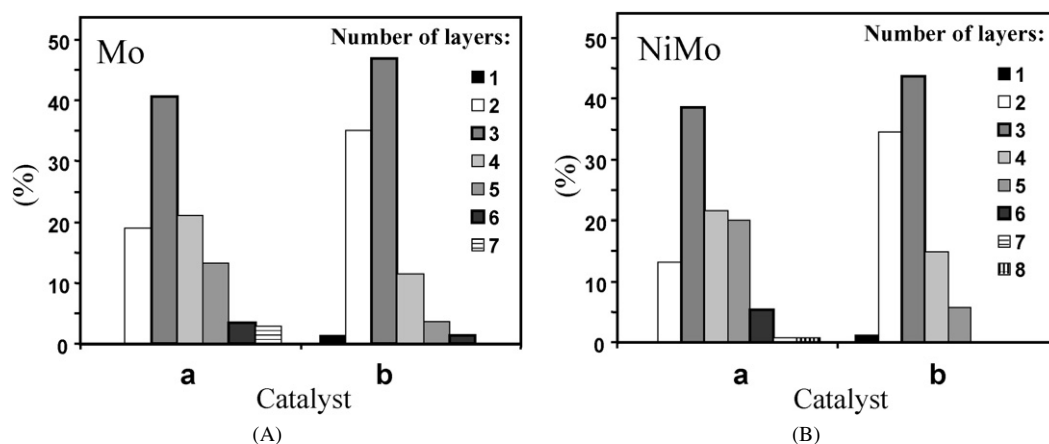


Fig. 12. Layer stacking distribution of MoS₂ crystallites in sulfided Mo (A) and NiMo (B) catalysts supported on SBA-15 (a); and Zr(23)SBA-15 (b).

as the support, the addition of Ni has only a slight effect on the morphology of MoS₂ particles. These results confirm that incorporation of zirconium into the support affects the dispersion of molybdenum active phase similar to that of a nickel promoter. In both cases, a more homogeneous distribution of smaller MoS₂ particles is obtained. It seems that ZrO₂ added in the SBA-15 support acts as a textural promoter for Mo catalysts.

3.3. Catalytic activity

In the present study, 4,6-dimethyldibenzothiophene, one of the most refractory sulfur compounds in gasoil [40], was selected as a model molecule to examine the catalytic activity of Mo and NiMo catalysts in deep HDS. The HDS of methyl-substituted DBT derivatives is known to occur through two parallel reactions (Fig. 14): (i) direct desulfurization (DDS),

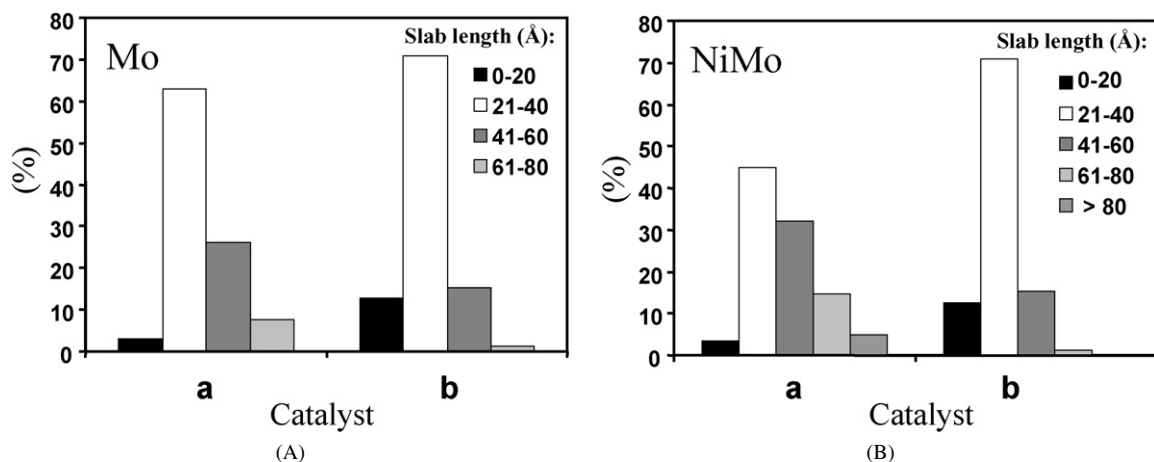


Fig. 13. Length distribution of MoS₂ crystallites in sulfided Mo (A) and NiMo (B) catalysts supported on SBA-15 (a); and Zr(23)SBA-15 (b).

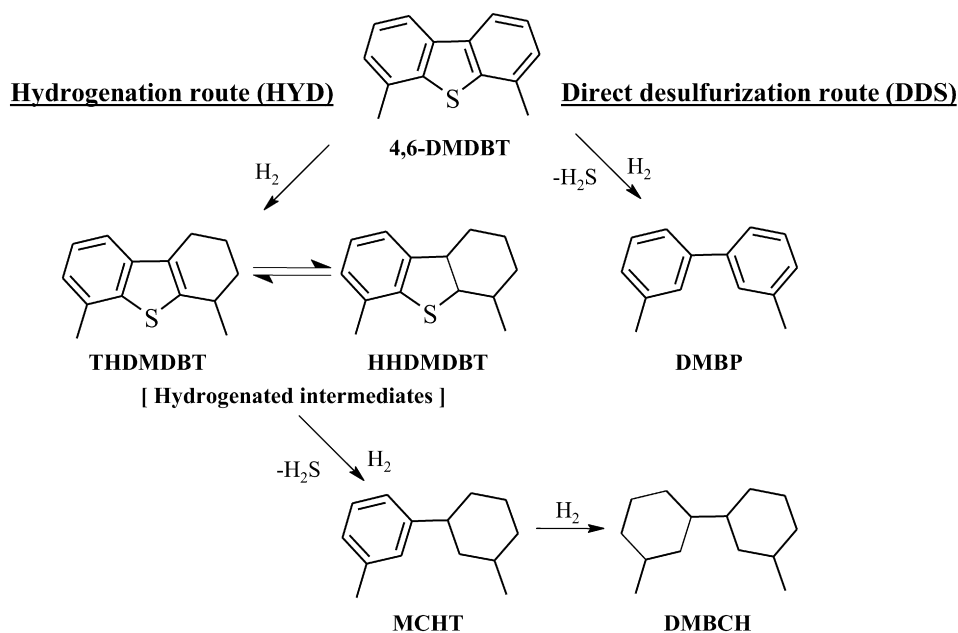


Fig. 14. Reaction scheme for the hydrodesulfurization of 4,6-DMDBT.

yielding the corresponding substituted biphenyl products, and (ii) hydrogenation with subsequent desulfurization (HYD), yielding first substituted tetrahydrodibenzothiophenes, then the corresponding hexahydro- derivatives and, finally, cyclohexylbenzene-type compounds [41,42]. It has been shown that under HDS conditions (i.e., in presence of an organic sulfur compound), biphenyl-type products do not readily hydrogenate into cyclohexylbenzene-type ones [43].

The conversions of 4,6-DMDBT obtained over Mo and NiMo catalysts supported on SBA-15 and Zr(*x*)SBA-15 materials are shown in Fig. 15. It can be observed that 4,6-DMDBT conversion reached at 8 h changes in a wide range. The lowest conversion (25%) was obtained with unpromoted Mo catalyst supported on siliceous SBA-15. The catalytic activities of all Mo catalysts supported on Zr(*x*)SBA-15 were significantly greater than that of the reference Mo/SBA-15 catalyst. Thus, 4,6-DMDBT conversions of 40–58% were obtained at 8 h of reaction time. Moreover, catalytic activity increased with in-

creasing ZrO₂ loading in the support, reaching a maximum with the sample prepared using the SBA-15 covered with a monolayer of Zr(IV) species [Zr(23)SBA-15]. The activity trend with the change in the ZrO₂ content in the support seems to be the result of the changes in the dispersion of Mo active species. As reported above, the incorporation of zirconia onto the SBA-15 surface provided better dispersion to oxidic and sulfided molybdenum phases. In addition, an increase in the proportion of easily reduced octahedrally coordinated Mo⁶⁺ species was found in Mo/SBA-15 catalysts after zirconia incorporation. Therefore, an increase in the total amount of HDS active sites can be expected in Mo catalysts supported on ZrO₂-modified SBA-15 materials compared with the corresponding pure silica support. This explains the increase in 4,6-DMDBT conversion with ZrO₂ loading seen in the Mo/Zr(*x*)SBA-15 catalysts.

Further increases in catalytic activity were seen after the incorporation of the Ni promoter into the Mo catalysts. 4,6-DMDBT conversions of 57–94% were obtained at 8 h of re-

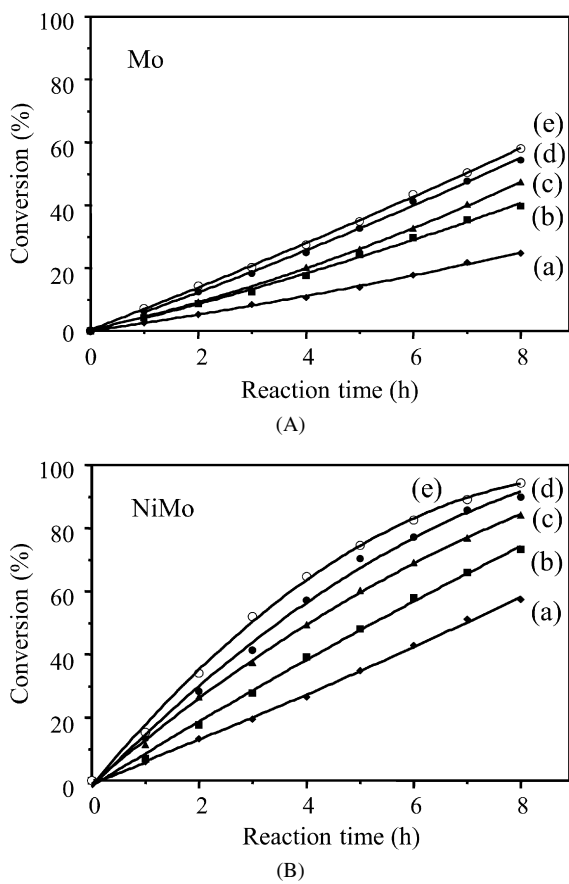


Fig. 15. 4,6-DMDBT conversions obtained over Mo (A) and NiMo (B) catalysts supported on SBA-15 (a); Zr(6)SBA-15 (b); Zr(13)SBA-15 (c); Zr(17)SBA-15 (d); and Zr(23)SBA-15 (e).

action time. The activity of NiMo catalysts followed the same trend with zirconia loading in the support as described above for unpromoted Mo catalysts; that is, the lowest 4,6-DMDBT conversion was obtained with the catalyst supported on siliceous SBA-15, and catalytic activity was increased with increasing ZrO₂ loading in the support. The 4,6-DMDBT conversions obtained with all NiMo/Zr(*x*)SBA-15 catalysts were significantly higher than that obtained with the reference NiMo/ γ -Al₂O₃ catalyst (61% at 8 h).

To elucidate the effect of Ni and ZrO₂ addition in Mo/SBA-15 catalysts on the reaction pathways of 4,6-DMDBT, the

reaction product distributions at the same total 4,6-DMDBT conversion (30%) were compared for different catalysts (Table 3). The ratios of the principal products of HYD and DDS routes (methylcyclohexyltoluene [MCHT] and dimethylbiphenyl [DMBP], respectively) from Table 3 show that for all catalysts studied, the preferential pathway is HYD. The proportion of MCHT increases with the incorporation of ZrO₂ into the support for both Mo and NiMo catalysts. The maximum MCHT/DMBP ratios (4.82 for the Mo catalyst and 7.68 for the NiMo catalyst) were reached with the catalysts supported on SBA-15 with the highest ZrO₂ loading (23 wt%). These catalysts were the most active in the Mo and NiMo series, respectively. Therefore, our results show that incorporation of ZrO₂ into the SBA-15 support leads to increased hydrogenation activity of Mo and NiMo catalysts, which promotes the HYD route of HDS of 4,6-DMDBT. This result is in line with a previous study [17] that found similar enhancement of HYD activity of NiMo catalysts when zirconium was added into mesoporous HMS silica support. In general, unpromoted Mo catalysts supported on ZrO₂-modified SBA-15 materials were found to be very active for the hydrogenation of the initial 4,6-dimethyldibenzothiophene; however, they were not able to efficiently eliminate sulfur from the hydrogenated intermediates (THDMDBT and HHDMDBT) obtained in the HYD route. Adding nickel to Mo catalysts resulted in a further increase in the MCHT/DMBP ratio, reflecting the change in the contributions of the DDS and the HYD pathways into the formation of the corresponding desulfurized products. In addition, incorporation of nickel into Mo catalysts resulted in a significant change in the product distribution of the HYD pathway (Table 3). In particular, the amounts of tetrahydro- and hexahydrodimethyldibenzothiophenes were much smaller (2–3 times smaller) with Ni-promoted catalysts than with the corresponding unpromoted ones. In line with this, the (THDMDBT + HHDMDBT)/MCHT ratio decreased significantly after Ni addition. Therefore, Ni increases the rate of sulfur elimination from hydrogenated intermediates of the HYD route. Previously it was shown that in the HDS of unsubstituted DBT, Ni enhances the rate of the direct desulfurization (DDS) pathway involving cleavage of the C–S bond in the starting reactant molecule [42]. Because the 4,6-DMDBT used in our study has steric constraints that hinder the DDS pathway, the increase in C–S bond cleavage was much more pronounced for the hy-

Table 3

Reaction product compositions obtained over Mo and NiMo catalysts at 30% of total 4,6-DMDBT conversion

Catalyst	t_{30}^a (h)	Product composition (%) ^b					Product ratio	
		TH	HH	DMBP	MCHT	DMBCH	(TH + HH)/MCHT	MCHT/DMBP
Mo/SBA-15	10	40.9	16.8	7.9	29.8	4.6	1.94	3.78
Mo/Zr(13)SBA-15	5.7	39.1	16.2	7.1	31.7	5.9	1.75	4.49
Mo/Zr(23)SBA-15	4.4	38.3	15.1	6.9	33.0	6.7	1.62	4.82
NiMo/SBA-15	4.5	26.8	9.1	10.1	46.6	7.4	0.77	4.63
NiMo/Zr(13)SBA-15	2.5	19.1	6.1	8.3	55.9	10.6	0.45	6.77
NiMo/Zr(23)SBA-15	1.8	16.2	5.6	7.7	59.2	11.3	0.37	7.68

^a Time in which 30% of 4,6-DMDBT conversion is reached.

^b TH (THDMDBT), tetrahydrodimethyldibenzothiophene; HH (HHDMDBT), hexahydrodimethyldibenzothiophene; DMBP, dimethylbiphenyl; MCHT, methylcyclohexyltoluene; DMBCH, dimethylbicyclohexyl.

drogenated intermediates of 4,6-DMDBT, products with no such steric hindrance as the initial 4,6-DMDBT. As a result, Ni addition strongly improved the overall kinetics of the HYD pathway of 4,6-DMDBT and produced only a slight increase in the DDS route. The general ability of Ni promoter to enhance the hydrogenolysis activity of Mo-based catalysts was previously attributed to different factors. The addition of nickel was supposed to decrease the strength of the bond between molybdenum and the sulfur atoms resulting from decomposition of the organic molecules or the metal–sulfur bond in the sulfide itself ([42] and references therein). Another possible factor is based on the increased electronic density and thus the basicity of the particular S^{2-} centers involved in the attack on the hydrogen atom (in β position relative to the sulfur atom in the organic molecule) leading to the C–S bond cleavage. It seems that our results confirm the conclusion of Bataille et al. [42] that a typical C–S bond cleavage center on a promoted catalyst should contain at least a promoter atom in the vicinity of a sulfide anion.

Returning to the previous observations, it can be concluded that zirconium(IV) incorporation into SBA-15 supports resulted in two principal effects: (i) increased overall catalyst activity due to better dispersion of Mo active species and (ii) enhanced hydrogenation ability of the catalysts. However, unpromoted Mo catalysts, even when supported on Zr-containing SBA-15 solids, are not able to efficiently realize the C–S bond cleavage, leading to sulfur elimination. The Ni promoter leads to further increase in MoS_2 dispersion, but the most important effect of nickel is the creation of active sites responsible for the C–S bond cleavage principally in prehydrogenated intermediate species obtained in the HYD pathway of the reaction (Fig. 14). Finally, the excellent activity of NiMo/Zr(23)SBA-15 catalyst for 4,6-DMDBT HDS can be attributed to its good hydrogenation ability induced by the incorporation of zirconia into SBA-15 support in combination with the high C–S bond cleavage activity enhanced by the addition of nickel.

4. Conclusion

Zirconia-containing SBA-15 materials with different ZrO_2 loadings (up to 23 wt%) were prepared by chemical grafting at room temperature. No considerable damage of the initial SBA-15 structure was observed after zirconia incorporation. Zirconia species were highly dispersed on the SBA-15 surface at both low and high, ZrO_2 loadings. The Zr–O–Si linkages formed during the grafting procedure were strong enough to resist thermal treatment at temperatures up to 800 °C. The presence of ZrO_2 species on SBA-15 surface significantly improved the hydrothermal stability of the material.

Results from XRD, DRS, TPR and HRTEM characterizations confirm that incorporation of zirconia into the SBA-15 support improved the dispersion of oxidic and sulfided Mo species, making their distribution more homogeneous. This finding demonstrates that zirconia acts as a textural promoter for Mo catalysts.

NiMo catalysts supported on ZrO_2 -containing SBA-15 molecular sieves showed high performance in the HDS of 4,6-

dimethyldibenzo thiophene. The activity trends with zirconia loading in the support were similar for unpromoted and Ni-promoted Mo catalysts. In both cases, increased overall catalyst activity was observed with zirconia loading, which can be attributed to better dispersion of the MoS_2 active phase with the corresponding increase in its effective surface. In addition, a detailed analysis of product distributions showed that adding ZrO_2 to the SBA-15 support also led to an increase in the catalysts' hydrogenation ability. Nevertheless, all unpromoted Mo catalysts, independent of the support used, were not able to efficiently realize the C–S bond cleavage, leading to sulfur elimination. Adding the nickel promoter resulted in a further increase in the dispersion of Mo oxidic species, making their reduction easier. However, the most important result of adding nickel to the Mo/SBA-15 catalysts was electronic modification of the active MoS_2 phase, resulting in the creation of active sites responsible for C–S bond hydrogenolysis principally in pre-hydrogenated intermediates obtained in the HYD pathway of the reaction. Finally, the greatest catalytic activity was obtained with the NiMo/Zr(23)SBA-15 catalyst, which showed the greatest hydrogenation ability induced by the incorporation of zirconia into the SBA-15 support in combination with the highest C–S bond cleavage activity enhanced by the addition of nickel.

Acknowledgments

Financial support was provided by CONACYT-Mexico (Grant 46354-Y). The authors thank M. Aguilar Franco, C. Salcedo Luna, and I. Puente Lee for technical assistance with the small-angle XRD, powder XRD, and HRTEM characterizations, respectively.

References

- [1] K.-H. Choi, N. Kunisada, Y. Korai, I. Mochida, K. Nakano, *Catal. Today* 86 (2003) 277.
- [2] G. Murali Dhar, G. Muthu Kumaran, M. Kumar, K.S. Rawat, L.D. Sharma, B. David Raju, K.S. Rama Rao, *Catal. Today* 99 (2005) 309.
- [3] M. Breyse, J.L. Portefaix, M. Vrinat, *Catal. Today* 10 (1991) 489.
- [4] M. Breyse, P. Afanasiev, C. Geantet, M. Vrinat, *Catal. Today* 86 (2003) 5.
- [5] H. Shimada, T. Sato, Y. Yoshimura, J. Hiraishi, A. Nishijima, *J. Catal.* 110 (1988) 275–284.
- [6] J.C. Duchet, M.J. Tilliette, D. Cornet, L. Vivier, G. Perot, L. Bekakra, C. Moreau, G. Szabo, *Catal. Today* 10 (1991) 579.
- [7] M. Vrinat, D. Hamon, M. Breyse, B. Durand, T. des Courieres, *Catal. Today* 20 (1994) 273.
- [8] M. Ji, P. Afanasiev, M. Vrinat, W. Li, C. Li, *Appl. Catal. A* 257 (2004) 157.
- [9] M. Jia, P. Afanasiev, M. Vrinat, W. Li, H. Xu, Q. Ge, *Petrochem. Tech.* 33 (2004) 202.
- [10] M. Vrinat, M. Breyse, C. Geantet, J. Ramirez, F. Massoth, *Catal. Lett.* 26 (1994) 25.
- [11] J. Ramirez, R. Cuevas, P. Castillo, M.L. Rojas, T. Klimova, *Bulg. Chem. Commun.* 30 (1998) 207.
- [12] F. Maugé, J.C. Duchet, J.C. Lavalley, S. Housenbay, E. Payen, J. Grimbrot, S. Kasztelan, *Catal. Today* 10 (1991) 561.
- [13] S. Damyanova, L. Petrov, P. Grange, *Appl. Catal. A* 239 (2003) 241.
- [14] E. Lecrenay, K. Sakanishi, I. Mochida, T. Suzuka, *Appl. Catal. A* 175 (1998) 237.

- [15] M.C. Barrera, M. Vinięra, J. Escobar, M. Vrinat, J.A. de los Reyes, F. Murrieta, J. García, *Catal. Today* 98 (2004) 131.
- [16] M.S. Rana, S.K. Maity, J. Ancheyta, G. Murali Dhar, T.S.R. Prasada Rao, *Appl. Catal. A* 268 (2004) 89.
- [17] N.G. Kostova, A.A. Spojakina, K. Jiratova, O. Solcova, L.D. Dimitrov, L.A. Petrov, *Catal. Today* 65 (2001) 217.
- [18] P.J. Kooyman, P. Waller, A.D. van Langeveld, C. Song, K.M. Reddy, J.A.R. van Veen, *Catal. Lett.* 90 (2003) 131.
- [19] Z. Li, L. Gao, S. Zheng, *Appl. Catal. A* 236 (2002) 163.
- [20] A.Y. Khodakov, V.L. Zholobenko, R. Bechara, D. Durand, *Microporous Mesoporous Mater.* 79 (2005) 29.
- [21] A. Sampieri, S. Pronier, J. Blanchard, M. Breyse, S. Brunet, K. Fajerwerg, C. Louis, G. Pérot, *Catal. Today* 107–108 (2005) 537.
- [22] D. Zhao, J. Feng, Q. Huo, N. Melosh, G.H. Fredrickson, B.F. Chmelka, G.D. Stucky, *Science* 279 (1998) 548.
- [23] D. Zhao, Q. Huo, J. Feng, B.F. Chmelka, G.D. Stucky, *J. Am. Chem. Soc.* 120 (1998) 6024.
- [24] O.Y. Gutiérrez, G.A. Fuentes, C. Salcedo, T. Klimova, *Catal. Today* 116 (2006) 485.
- [25] T. Yamada, H. Zhou, K. Asai, I. Honma, *Mater. Lett.* 56 (2002) 93.
- [26] I.G. Shenderovich, G. Buntkowsky, A. Schreiber, E. Gedat, S. Sharif, J. Albrecht, N.S. Golubev, G.H. Findenegg, H.-H. Limbach, *J. Phys. Chem. B* 107 (2003) 11924.
- [27] T. Klimova, M.L. Rojas, P. Castillo, R. Cuevas, J. Ramirez, *Microporous Mesoporous Mater.* 20 (1998) 293.
- [28] R. Mokaya, *J. Phys. Chem. B* 103 (1999) 10204.
- [29] Q.-H. Xia, K. Hidajat, S. Kawi, *Mater. Lett.* 42 (2000) 102.
- [30] S. Kawi, S.-C. Shen, *Mater. Lett.* 42 (2000) 108.
- [31] T. Klimova, M. Calderón, J. Ramirez, *Appl. Catal. A* 240 (2003) 29.
- [32] C.C. Williams, J.G. Ekerdt, J.-M. Jehng, F.D. Hardcastle, A.M. Turek, I.E. Wachs, *J. Phys. Chem.* 95 (1991) 8781.
- [33] C.C. Williams, J.G. Ekerdt, J.-M. Jehng, F.D. Hardcastle, I.E. Wachs, *J. Phys. Chem.* 95 (1991) 8791.
- [34] M. Henker, K.-P. Wendlandt, J. Valyon, P. Bornmann, *Appl. Catal.* 69 (1991) 205.
- [35] B. Scheffer, J.J. Heijinga, J.A. Moulijn, *J. Phys. Chem.* 91 (1987) 4752.
- [36] R. López Cordero, A. López Agudo, *Appl. Catal. A* 202 (2000) 23.
- [37] R. López Cordero, F.J. Gil Llambias, A. López Agudo, *Appl. Catal.* 74 (1991) 125.
- [38] S. Damyanova, A. Spojakina, K. Jiratova, *Appl. Catal. A* 125 (1995) 257.
- [39] C. Louis, M. Che, M. Anpo, *J. Catal.* 141 (1993) 453.
- [40] B.C. Gates, H. Topsøe, *Polyhedron* 16 (1997) 3213.
- [41] C. Pophal, F. Kameda, K. Hoshino, S. Yoshinaka, K. Segawa, *Catal. Today* 39 (1997) 21.
- [42] F. Bataille, J.L. Lemberon, P. Michaud, G. Pérot, M. Vrinat, M. Lemaire, E. Schulz, M. Breyse, S. Kasztelan, *J. Catal.* 191 (2000) 409.
- [43] P. Michaud, J.L. Lemberon, G. Pérot, *Appl. Catal. A* 169 (1998) 343.